JGR Space Physics

RESEARCH ARTICLE
10.1029/2019JA027702

Average Ionospheric Middle and Low Latitudes Nighttime Zonal Currents Deduced From CHAMP

Yun-Liang Zhou[1], **Hermann Lühr**[2], **and Patrick Alken**[3]

[1]Department of Space Physics, School of Electronic Information, Wuhan University, Wuhan, China, [2]GFZ, German Research Centre for Geosciences, Section 2.3, Geomagnetism, Potsdam, Germany, [3]Cooperative Institute for Research in Environmental Sciences, University of Colorado, Boulder, CO, USA

Key Points:
- Height-integrated current densities of nighttime zonal ionospheric currents at middle and low latitudes are deduced from magnetic signatures
- The first comprehensive study of nighttime ionospheric current distributions at F-region altitudes is presented
- The westward EEJ at E-region is detected during postmidnight/early morning hours, showing a clear wave-1 longitudinal pattern

Supporting Information:
- Supporting Information S1

Correspondence to:
Y.-L. Zhou,
zhouyl@whu.edu.cn

Citation:
Zhou, Y.-L., Lühr, H., & Alken, P. (2020). Average ionospheric middle and low latitudes nighttime zonal currents deduced from CHAMP. *Journal of Geophysical Research: Space Physics*, *125*, e2019JA027702. https://doi.org/10.1029/2019JA027702

Received 4 DEC 2019
Accepted 30 JUN 2020
Accepted article online 17 JUL 2020

Abstract By utilizing magnetic field measurements collected by CHAMP during the years 2001–2009, average characteristics of nighttime ionospheric zonal currents at middle and low latitudes are investigated. We provide for the first time the detailed dependencies of these currents on location, local time, season, and the level of solar activity. The main results obtained are (1) the nighttime zonal ionospheric currents at F-region altitude, derived from the vertical magnetic component, exhibit on average height-integrated current densities up to 10 mA/m. The amplitude varies quasi-linearly with F10.7 flux level. (2) During equinoxes symmetric current systems at F-region altitude are found in the two hemispheres. After sunset, eastward currents dominate at low latitudes, fading away toward midnight. After midnight regions of eastward currents are observed at midlatitude. During solstice seasons, eastward currents are enhanced in the summer hemisphere; westward currents are stronger in local winter. (3) Longitudinal variations of F-region currents show clear wave-1 patterns. This is related to the effect of the stationary planetary wave-1 and the diurnal nonmigrating tide, D0. This dominant tidal signal, enhancing eastward currents over the Pacific region, appears at middle and low latitudes and during all seasons. (4) At the magnetic equator, signs of the equatorial electrojet (EEJ) are evident after 02:30 MLT. Intensity of westward currents in the narrow band increases toward sunrise. Longitudinal variations of the EEJ show a similar wave-1 pattern as F-region currents. Here the westward current density is enhanced over Africa/India. The EEJ wave-1 modulation is strongest around June solstice.

1. Introduction

Under the influence of solar extreme ultraviolet (EUV) and X-ray radiation part of the Earth's upper atmosphere is ionized, forming the ionosphere. According to the variation of electron density with altitude, the ionosphere is divided into three layers, D, E, and F (Kelley, 2009). At night, the ionospheric conditions differ significantly from that on the dayside. Shortly after sunset the D-layer disappears, and the electron density in the E-region rapidly decreases. The F-region, however, maintains enough ionization throughout the night to support current flow, detectable by satellite measurements. In this study the nighttime hours are of interest.

The intensity of electric currents in the ionosphere is proportional to the content of charged particles. At night the highest electron density occurs at the F-region peak, which can be found at altitudes around 300 km depending on the level of solar activity. This is the altitude range at which the primary nighttime currents are expected. Any force acting on the charge carriers contributes to the current, for example, electric field, wind, pressure, and gravity. In the F-region and in particular at night, the electric field is not so efficient because it moves electrons and ions in the same direction. The thermospheric winds drag ions across geomagnetic field lines, driving dynamo currents (Fejer, 2011; Heelis, 2004; Richmond, 1979). The large-scale F-region neutral winds blow from the dayside to the nightside, resulting from the enhanced pressure on the sunlit dayside. A plasma pressure gradient drives currents perpendicular to the ambient magnetic field and to the gradient. Largest effects are expected in the vicinity of the equatorial ionization anomaly (EIA). Gravity-driven currents in the F-region are directed eastward (e.g., Kelley, 2009). They are most prominent at low latitudes, where the magnetic inclination is low, and they maximize slightly above the F-region peak. For reviews on these current systems see, for example, Alken et al. (2017) and Maute and Richmond (2017). Zonal winds near the magnetic equator drive vertical currents in the F-region, which were first predicted by Rishbeth (1971a, 1971b) and later confirmed by Maeda et al. (1982) based on Magsat magnetic field data. In this study we focus on zonal ionospheric currents.

The existence of horizontal F-region currents at middle latitudes on the nightside has earlier been detected from satellite measurements at two altitudes. Shore et al. (2013) employed coordinated magnetic field recordings from Ørsted and CHAMP for estimating the mean zonal current density in the layer between about 400 and 700 km altitude. The results are very scattered, but they reported current densities of less than 0.1 $\mu A/m^2$. Tozzi et al. (2015) made use of the Swarm satellite constellation for determining in a statistical sense the mean zonal current density flowing between the Swarm A and C satellite pair at 460 km altitude and the 50 km higher Swarm B. They reported for middle and low latitudes mean westward currents with a density of about 10 nA/m^2 for the premidnight hours (19–23 LT) and half of that value after midnight (01–05 LT). Lühr et al. (2016) also utilized the Swarm magnetic field observations at these two altitudes for current density estimation by applying Ampère's law in ring integral form on an orbit-by-orbit basis. They also found dominating westward currents at nighttime with densities around 10 nA/m^2. Only at some regions, mainly in the southern hemisphere, eastward currents are detected. All of the above studies probed a fairly high-altitude range, while F-region currents at night are expected to peak at altitudes around 300 km. Therefore, the mentioned studies missed the main part of the zonal currents.

Another topic of this study is the behavior of the equatorial electrojet (EEJ) at nighttime. This has never been studied in detail. The EEJ manifests itself as a narrow ribbon of intense current density along the magnetic equator in the E-region. The confinement is caused by high Cowling conductivity in the E-region where the geomagnetic field lines are close to horizontal. The high electrical conductivity diminishes rapidly above and below the E-layer allowing a vertical electric field to build up (see Kelley, 2009). This situation is fulfilled in the sunlit hemisphere. The situation on the nightside is not so well known.

During daytime the EEJ current is typically flowing eastward, following the large-scale electric field. When studying the properties of the westward electrojet Zhou, Lühr, Xu, et al. (2018) found that the so-called counter electrojet (CEJ) occurs about 90% of the time at local times around 06 MLT. This is consistent with the westward direction of the large-scale E-field at that local time. For this reason, it is expected that the westward electrojet will dominate also at times before sunrise. To our knowledge, so far, no study has focused on the predawn electrojet and its properties.

For a detailed investigation of the nightside ionospheric currents we make use of the high-resolution magnetic field measurements collected by the CHAMP satellite during 2001–2009. This large data set allows for resolving the mean characteristics of those currents including their spatial, temporal, and seasonal dependences.

In the sections to follow, we first introduce the data set and the processing method. The features of the magnetic signal caused by the nighttime ionospheric currents will be outlined in section 3. In section 4 we present the zonal current density inverted from the vertical magnetic field component. Investigated features include the seasonal dependence and longitudinal variation of the nighttime zonal currents. Mean characteristics of the EEJ during dark hours will be shown in section 5. In section 6, the obtained results will then be discussed in the context of previous publications. Main findings are summarized and conclusions are drawn in section 7.

2. Data and Processing

2.1. CHAMP Data Set

The data set we used for the study of nighttime ionospheric currents is mainly from the measurements taken by CHAMP satellite (CHAllenging Minisatellite Payload), which was launched on 15 July 2000 into a circular and near polar orbit with an initial altitude of 454 km (Reigber et al., 2002). By the end of the mission, in September 2010, its orbit decayed to about 250 km. CHAMP needed about 131 days to sample all local times when considering the upleg (northbound) and downleg (southbound) arcs. During the 10-year mission time, the onboard magnetometers, including the Fluxgate Magnetometer (FGM) and the absolute scalar Overhauser Magnetometer (OVM), provided a wealth of magnetic field observations with high precision and wide coverage, allowing to investigate the characteristics of ionospheric currents. The FGM vector magnetic field readings are calibrated routinely by using the observations of the onboard absolute scalar Overhauser Magnetometer as a reference. In this paper, the fully calibrated Level-3 magnetic field products (product identifier: CH-ME-3-MAG) are used (Rother & Michaelis, 2019), which provide the magnetic field

recordings with time resolution of 1 s in the North-East-Center (NEC) frame. Besides the magnetometers, CHAMP was also equipped with a Langmuir probe, which offered the measurements of electron density and temperature.

2.2. Processing of Magnetic Field Data

For investigating the features of nighttime ionospheric currents, we utilized the magnetic field measurements from the FGM and OVM onboard CHAMP. In order to isolate the magnetic effects caused by ionospheric currents, the main, crustal, and magnetospheric fields are removed from the vector and total magnetic field measurements by subtracting the latest version of the CHAOS-6 model (Finlay et al., 2016). The CHAOS-6 model is a time-dependent geomagnetic field model, which represents the contributions from the geodynamo in the core, crustal magnetization, and the large-scale magnetospheric fields at any location up to 1,000 km.

In addition, a correction of the diamagnetic effect, produced by small- and medium-scale pressure gradients in the ambient plasma, is applied to the magnetic field residuals. The required correction of the total field, b, follows the approach of Lühr et al. (2003), which can be written as

$$b = -nk(T_i + T_e)\frac{\mu_0}{B} \tag{1}$$

where n is the electron number density, k is the Boltzmann constant, T_i and T_e are the ion and electron temperatures, respectively, μ_0 is the susceptibility of free space, and B is the ambient magnetic field strength. Here the plasma density and temperature measurements are from the Langmuir probe onboard CHAMP. For a more detailed description of the diamagnetic effect correction, the reader is referred to Zhou, Lühr, and Alken (2018) and Zhou, Lühr, Xu, et al. (2018). After splitting the diamagnetic effect, b, of the total field proportionally among the components, these values are subtracted from the residuals. The resulting vector magnetic fields, ΔBx, ΔBy, and ΔBz, and scalar residual, ΔB, are the basis for our ionospheric current study. Here ΔBx, ΔBy, and ΔBz are the northward, eastward, and downward components of the magnetic field residuals.

The residuals of the magnetic data are grouped into different magnetic local time (MLT) bins, using the MLT at which CHAMP crossed the equator on its pass. Data from these passes are sorted into 24 MLT bins with a width of 1 hr. Then the residuals in each MLT bin are further subdivided in Quasi-Dipole latitude (QDlat) bins at 1° resolution. The Quasi-Dipole coordinates are appropriate for interpreting ionospheric currents (Richmond, 1995). Since we focus in this study on currents at middle and low latitudes, the considered latitudes are ranging from −45° to 45° QDlat. After the sorting and stacking, the residuals in the 1 hr MLT by 1° QDlat bins are averaged. Finally, the averaged magnetic residuals of neighboring QDlat bins are smoothed in the direction of QDlat, for eliminating apparent small-scale variations. For smoothing we use the formula

$$y(n) = 0.25x(n-1) + 0.5x(n) + 0.25x(n+1) \tag{2}$$

where $x(n-1)$, $x(n)$, and $x(n+1)$ denote the value of the previous, current, and next bin in a latitudinal profile, respectively. $y(n)$ is the smoothed residual value.

3. Average Magnetic Field Profiles

For obtaining the mean features of magnetic signals caused by the ionospheric currents, we took into account data from the years ranging from 2001 to 2009. Due to a changed flight attitude at the end of the CHAMP mission, no plasma data are available for the year 2010; thus the diamagnetic correction could not be performed. Considering that the orbit plane covered 24 hr in local time in 131 days, CHAMP sampled all local time just 14 times in 5 years, providing an even local time coverage during all seasons. Accounting for the varying solar activity level, we divided the 9-year period into two 5-year periods with 1 year of overlap, namely, 2001–2005 and 2005–2009. The first 5-year period experienced high to moderate solar activity levels, while during the second 5-year period low activity was dominating. The average radio flux index F10.7 values are 137.4 sfu and 76.9 sfu for the first and second 5-year periods, respectively. The aforementioned split of the considered time period gives us the opportunity to compare the response of the ionospheric currents to the solar radiation level. For more detailed comparisons, we also checked the geomagnetic activities

of these two periods. Mean Ap values are 14.9 nT (8.0 nT) for the first (second) period. Finally, the orbital altitude was changing during the periods because of the orbit decay. Resulting CHAMP mean altitudes are 396.4 and 347.8 km for the years 2001–2005 and 2005–2009, respectively.

3.1. Example Profiles

According to Equation (2) in Lühr et al. (2004), the magnetic effect of a zonal current element in the horizontal component depends strongly on its height above or below the measure point

$$\Delta Bx = -\frac{\mu_0 I}{2\pi} \cdot \frac{h}{x^2 + h^2} \tag{3}$$

where ΔBx is the northward component of the magnetic field caused by the current, I is the current strength of the eastward current, μ_0 is the permeability of free space, h is the height of the measurement point above the current, and x is the southward displace of the sampling point. If the satellite flies at the center of a current sheet, the observed horizontal signal is zero. The sign of the horizontal magnetic signal change when the satellite crosses the center height. At night, the ionospheric fields mainly come from F-region currents. According to the orbit altitude during the periods we considered, CHAMP had probably sampled magnetic fields inside the current layer. Therefore, the horizontal component, ΔBx, is not providing enough information for deriving the current direction and intensity. On the other hand, the vertical component, ΔBz, is much more suitable. Its signature varies little with the height difference between current center and measurement. Thus, the variation of CHAMP orbital altitude through the mission has little influence on the signatures of the vertical component. Moreover, the gradient of the vertical component is proportional to the height-integrated current density and its sign determines the current direction. For more details about the relation between ΔBz variation and current distribution see section 4.1 and the description in the supporting information. Therefore, in this study we will mainly focus on the signatures in the vertical component. In addition, the residuals of the scalar magnetic field, ΔB, are also considered for obtaining additional information about the various currents contributing to the observations. Note that at low latitudes ΔB and ΔBx exhibit almost the same variations.

Figure 1 presents the average latitudinal variations of the vertical component and scalar magnetic field, which are labeled as ΔBz and ΔB, at different MLTs (19, 24, and 05 MLT) for the periods 2001–2005 and 2005–2009. The curves represent the averages of observations from one local time hour, centered on the start of the noted hour (e.g., from 18:30 to 19:30 for 19 MLT). Figure 1 depicts some general characteristics of the magnetic signal caused by the ionospheric currents during nighttime. From these graphs we can get an impression of the current configuration. Let us first have a look at the period of 2001–2005. In Figure 1a we see that ΔB is negative for 19 MLT, having a peak amplitude of about −5.1 nT at 0° QDlat. And the variation of ΔB is rather symmetric about the magnetic equator. On the other hand, ΔBz (see Figure 1b) decreases from about 1.0 to −2.4 nT within ±15° QDlat, showing a negative slope. This implies an eastward current flowing within this region. The mean positions of the current borders in northern and southern hemispheres appear at ±15° QDlat, colocated with the positive and negative peaks of ΔBz. Furthermore, the negative sign of ΔB combined with the negative slope of ΔBz suggests that CHAMP passed above the current sheet center. For 00 MLT, Figure 1c indicates that ΔB is mainly positive with a peak-to-peak value of about 2.0 nT, which is smaller than that at 19 MLT. Similarly, ΔBz at 00 MLT (see Figure 1d) also shows a smaller amplitude than that at 19 MLT, which implies weaker currents. And the sign of the slope in ΔBz around 0° QDlat is positive, different from that of 19 MLT. This reflects weak westward currents.

Now we turn to 05 MLT. It can be seen from Figure 1e that ΔB is positive with a peak-to-peak value of about 4.3 nT. Interestingly, there is a clear bump near 0° in QDlat. We relate this bump to the effect of the EEJ. A more detailed justification for it is given in section 5. From Figure 1f one can see that ΔBz changes from about −2.4 to 1.6 nT within ±15° in QDlat, showing a steep positively signed slope. This demonstrates that at 05 MLT a stronger ionospheric current is flowing westward at low latitudes. From the combination of positive slope and positive ΔB it can be deduced that CHAMP flew again above the current center. From all these variations of the magnetic data we imply that on average there exists at low latitudes an eastward current in the ionospheric F-region after sunset. Around midnight the current almost vanishes and changes direction from eastward to westward. This low latitude westward current becomes stronger toward early morning hours. During the period 2005–2009, the mean magnetic signatures (see Figures 1g–1l) are

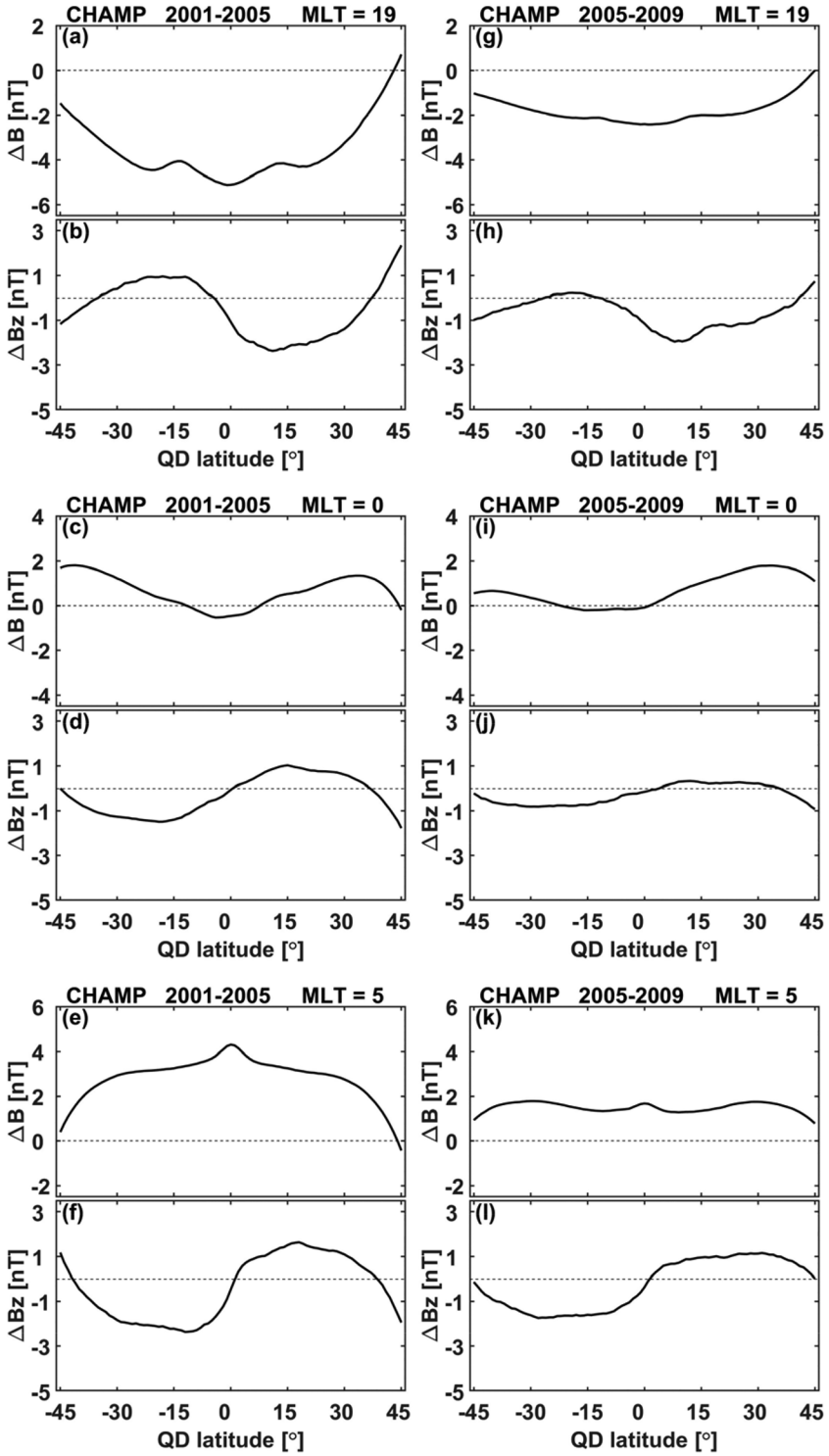

Figure 1. Mean latitudinal variations of the total magnetic field residuals, Δ*B* and of the vertical component, Δ*Bz* for three nighttime MLT hours from the periods 2001–2005 and 2005–2009.

similar to those from 2001 to 2005, but they exhibiting smaller amplitudes. We can again deduce eastward low latitude currents at late evening, turning westward in the postmidnight sector. From the pairing of *ΔB* sign and *ΔBz* slope we conclude that CHAMP cruised above the current sheet center in all cases.

Estimated current densities are here about a factor of 2 smaller. This is attributed to the lower solar EUV radiation level during 2005–2009.

3.2. Geomagnetic Activity Dependence

Having seen the general characteristics of the variations in ΔBz and ΔB at nighttime, we now check the dependence of the magnetic variation on geomagnetic activity. For deriving the dependence of ΔBz and ΔB on the geomagnetic activity, we restricted the selection to Kp $\leq$ 2 for magnetically quiet times and Kp $\geq$ 4 for active times. Figure 2 shows the latitudinal variations of the residuals in ΔBz and ΔB for quiet and active times at different MLTs during 2001–2005. Our later time period is not suitable for this investigation because it contains too few high-activity samples.

For quiet times, it can be seen in Figures 2a–2f that the variation characteristics of ΔBz and ΔB are similar to that of Figures 1g–1l but showing smaller amplitude (in particular for ΔB). For the magnetically active times, the situation is complicated, and the residuals changed remarkably. This can be seen from Figures 2g–2l at the three selected MLTs for Kp $\geq$ 4. The most prominent impression is that the amplitude of ΔB is enhanced greatly. In principle, CHAOS-6 should correct also for the influence of the ring current, but at a larger activity it seems not to account properly for all the ring current effects. According to Finlay et al. (2016), the model is based only on data from quiet times (Kp < 2). We thus assume that most of the observed phenomena during active times are related to an insufficient correction of the ring current effect by the CHAOS-6 model. Confirmation for the assumption is provided by Lühr and Zhou (2020).

Generally, the symmetric ring current causes a magnetic effect at Earth surface similar at all longitudes. But at magnetically active times, in particular during the main phase of a geomagnetic storm, asymmetric parts appear (e.g., Le et al., 2011). The asymmetric distribution of current, namely, the partial ring current effect, causes stronger magnetic deflections at certain local times. Depending on the level of magnetic activity the storm-time disturbance is enhanced around the 18 MLT sector and reduced around 06 MLT (e.g., Lühr et al., 2017). Just such effects can be seen in the plots for magnetic deflections during disturbed periods (Kp > 4) in Figures 2g–2l. For example, ΔB exhibits large negative deflections at 19 MLT (panel g), that is, an underestimation of the ring current effect around this local time, and ΔB shows positive deflections at 05 MLT (panel k), which means an overestimation by CHAOS-6.

To first order, the ring current causes a homogeneous magnetic field at the Earth that is aligned with the dipole axis, as expected in the center of a large ring. This homogeneous field adds to the dipole field of the Earth. The resulting modification of the scalar magnetic field can be expressed as the scalar product between the vector fields of the ring current, B_{RC} and the Earth's dipole, B_{Dipole}, normalized by the total field strength. The result can be written as $\Delta B = B_{RC} \cdot (3sin^2\beta - 1)/\sqrt{1 + 3sin^2\beta}$, here B_{RC} is the magnitude of the magnetic field caused by the ring current at the geomagnetic equator, and β is the dipole latitude. According to the above formula the magnetic effects produced by the ring current is fully reflected by ΔB at $\beta = 0$, and the ΔB signal vanishes at $\pm$35.26° QDlat where we have $3\sin^2\beta - 1 = 0$. From the curves in Figures 2g, 2i, and 2k we can estimate that after the field removals by CHAOS-6 a residual average ring current effect exists, which amounts to about −13.4 nT at 19 MLT, −7.0 nT at 00 MLT, and +5.7 nT at 05 MLT. This clearly indicates that CHAOS-6 is not able to remove for magnetically active conditions properly the effect of the partial ring current. The residual ring current effect can also be seen in ΔBz variations (Figures 2h, 2j, and 2l). For this component we expect $\Delta Bz = B_{RC} \sin\beta$. This implies that a nearly linear field gradient is added at low latitudes. The curve of ΔBz shows clearly the effect of an additional positive slope for the 19 MLT case and a negative slope for 05 MLT during disturbed periods. For more details about residual to the CHAOS-6 model the reader is referred to the study by Lühr and Zhou (2020). The obvious residual effects of the ring current make it difficult to deduce proper estimates of F-region nighttime currents. We thus have excluded all CHAMP measurements from times with Kp > 4 from our analysis.

3.3. Seasonal Dependence

So far, we considered only the annual averages of the magnetic effects of the nighttime ionospheric current. As reported by Maus and Lühr (2006), there are seasonal dependences in the magnetic signal caused by ionospheric currents at 20–22 LT. For investigating the seasonal variations of the magnetic effects from ionospheric currents over the entire nighttime, we grouped the magnetic signals into June solstice and December solstice seasons by considering in both cases the 131 days centered on 1 July and 1 January,

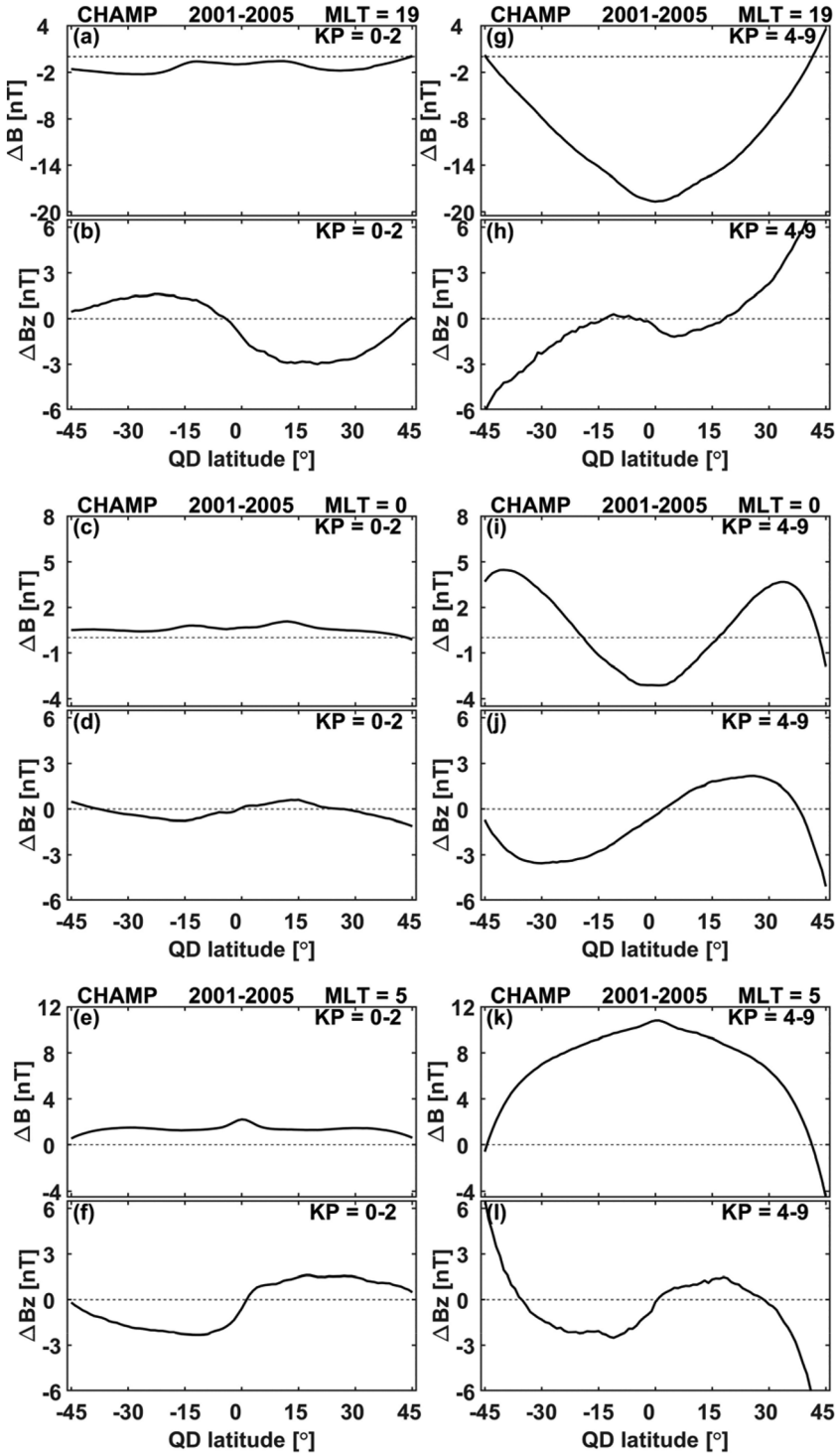

Figure 2. Mean latitudinal variations of the total magnetic field and the vertical component residuals for three nighttime MLT hours from the period 2001–2005 (left) for low (Kp = 0–2) and (right) high (Kp = 4–9) geomagnetic activity.

respectively. Because of the prominent ring current signal in the residual, as shown in the previous subsection, we limit all further analysis to quiet and moderately active periods (Kp = 0–4), which is a compromise between a sufficiently large number of samples and avoiding ring current effects.

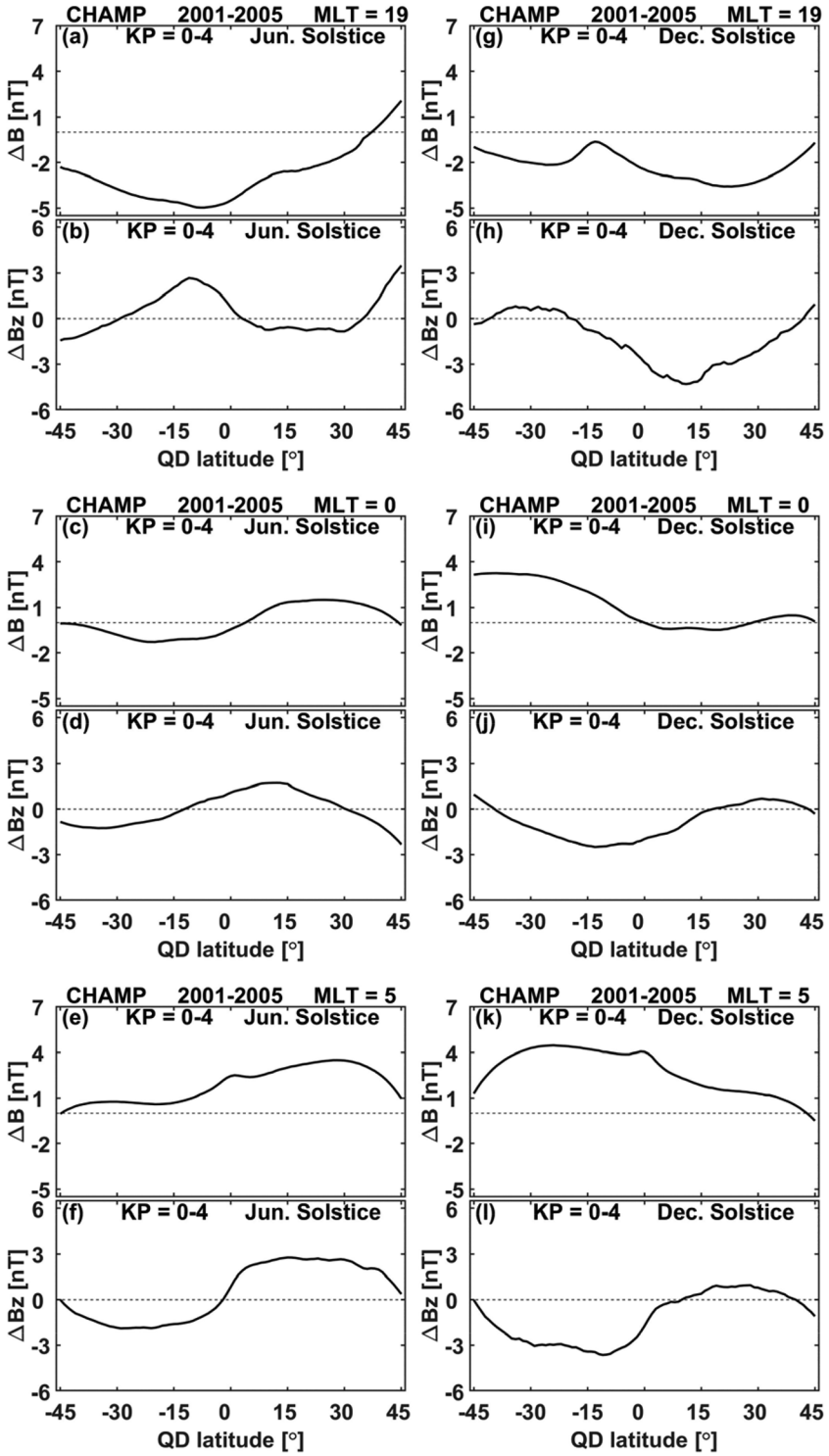

Figure 3. Mean latitudinal variations of the total magnetic field and the vertical component residuals for three nighttime MLT hours from the period 2001–2005 (left) for June solstice and (right) December solstice.

Figure 3 displays the latitudinal variations of the residuals in ΔBz and ΔB at different MLTs during 2001–2005 from June and December solstice seasons. For 19 MLT we can see in Figure 3a (June solstice) that the residuals of the scalar magnetic data are mainly negative, which is similar to Figure 1a. But it shows

an asymmetric latitudinal variation where the more negative magnetic signal appears in the southern hemisphere. From Figure 3b the latitudinally asymmetric variations of ΔBz can also be deduced. The prominent positive peak in ΔBz (2.7 nT) is appearing at −11° QDlat, and the zero crossing of the negative slope (latitudinal center of the current) is shifted into the northern hemisphere, into local summer conditions. Similar to Figure 1b, the negative gradient of ΔBz reflects an eastward ionospheric current at low latitudes. For December solstice, we can see from Figure 3g that the minimum amplitude in ΔB at 23° QDlat also appears in local winter with an amplitude of about −3.6 nT. And the prominent negative peak of ΔBz (see Figure 3h) is found during this season at 11° QDlat, also winter hemisphere. In this case the latitudinal center of the ionospheric current (zero crossing of negative slope) at 19 MLT has shifted about 11° in QDlat to the southern summer hemisphere.

At 00 MLT (Figures 3c, 3d, 3i, and 3j) the variations of ΔB and ΔBz in general are small, but still we find also here a clear asymmetry of the curves between the two seasons with respect to equatorial latitudes.

Around 05 MLT (see Figures 3e, 3f, 3k, and 3l) the situation changed greatly compared to 19 MLT. Firstly, ΔB is totally positive in both hemispheres, showing the bump at 0° QDlat again. The maximum amplitude of ΔB, 3.5 nT (4.5 nT), appears in local summer at 28° (−24°) QDlat around June (December) solstice season. The positive sign of the gradient in ΔBz near the magnetic equator indicates a westward ionospheric current at low latitudes. Furthermore, the peak amplitude of the bipolar ΔBz variations, −1.9 (2.8) nT and −3.6 (1.0) nT in southern (northern) hemisphere, is clearly larger in the summer hemisphere during both seasons. This indicates stronger eastward currents in the summer than in the winter hemisphere at middle latitudes during early morning hours.

4. Average F-Region Current Distribution

Having seen the features of the magnetic signals caused by the nighttime ionospheric currents, we may want to get a qualitative impression of the current configuration. For better understanding the characteristics of the current at night, we regard the current density as a more suitable parameter. Considering that CHAMP flew inside the F-region current sheet, the horizontal component and scalar magnetic field residuals provide no unique information about the current intensity. While on the other hand the height difference between CHAMP and the ionospheric current sheet center has little influence on the variations of the vertical magnetic field component. Thus, we attempt to invert the current density from the ΔBz latitudinal profiles. In the next section, we will first describe the inversion approach. Then, we inspect the dependences of the current density on season, solar activity level, and longitude.

4.1. Deriving Current Density From Magnetic Field Profiles

For deriving the current density, the nighttime ionospheric currents at middle and low latitudes are assumed to flow near the F-region peak. We represent the currents by a series of 99 east–west line currents (perpendicular to the orbit) separated by 1° in latitude within the ±49° QDlat range. In order to invert the ionospheric current density, magnetic field measurements, taken by CHAMP at latitudes spanning from −50° to 50° QDlat, are utilized. Figure 4 shows a schematic illustration of the envisaged ionospheric currents at middle and low latitudes and the CHAMP orbit. In this graph, the thick dashed-dotted arc with a radius of R_{cur} denotes the current layer center, assumed to be located 50 km below CHAMP's orbit, which is indicated by a thin outer arc. From the observed relation between ΔB and ΔBz signatures we know that the current centers in all the presented cases are located slightly below the CHAMP orbit. The letter i denotes the ith CHAMP measurements, and the letter j denotes a line current at the jth QDlat. The label $\Delta\beta(i,j)$ represents the latitude difference in QDlat between the ith measurement point and the jth line current, namely, $\Delta\beta(i, j) = \beta(j) - \beta(i)$.

The vertical magnetic field variation caused by an east-directed line current at CHAMP orbital altitude can be written as (e.g., Lühr et al., 2004)

$$\Delta Bz = \frac{\mu_0 I}{2\pi} \cdot \frac{x}{x^2 + h^2} \tag{4}$$

here ΔBz is the downward component of the magnetic field caused by the current, I is the current strength of the eastward current, μ_0 is the permeability of free space, h is the height of the measurement point

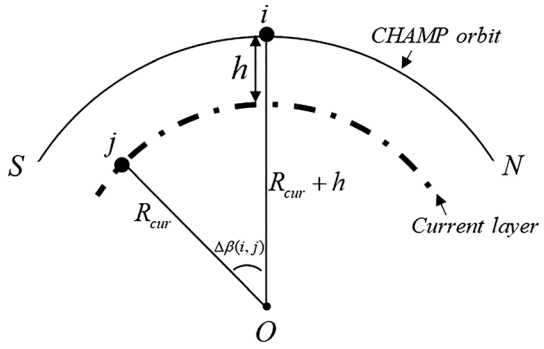

Figure 4. Schematic drawing of the configuration for the ionospheric current estimation. The center of the F-region zonal current layer is assumed to be located 50 km below the CHAMP orbit.

above the line current, and x the southward displace of the CHAMP position from the current. If we consider multiple currents, the effect at the ith measurement point and from the jth line current, causing the downward component, $\Delta Bz(i,j)$, is given as

$$\Delta Bz(i,j)=\frac{\mu_0}{2\pi}\cdot J(j)\cdot\Delta l\cdot\frac{x(i,j)}{x^2(i,j)+h^2(i,j)} \tag{5}$$

where $J(j)$ is the height-integrated current density representing the jth line current, and Δl is the distance between lines (here 110 km for 1° QDlat), $x(i,j)=R_{cur}\cdot\sin(\Delta\beta(i,j))$ and $h(i,j)=50+R_{cur}\cdot[1-\cos(\Delta\beta(i,j))]$ both in units of km. Thus, the total downward component effect at the ith measurement point, caused by the 99 line currents, can be expressed as

$$\Delta Bz(i)=\frac{\mu_0}{2\pi}\sum_{j=1}^{m}\left[\frac{x(i,j)\cdot\Delta l}{x^2(i,j)+h^2(i,j)}J(j)\right] \tag{6}$$

here m is 99, denoting the number of the line currents. For solving the current density of all line currents, we write Equation 6 into the matrix form as

$$\begin{bmatrix}\Delta Bz(1)\\ \Delta Bz(2)\\ \dots\\ \Delta Bz(n)\end{bmatrix}=\begin{bmatrix}A(1,1) & A(1,2) & \dots & A(1,m)\\ A(2,1) & A(2,2) & \dots & A(2,m)\\ \dots & \dots & \dots & \dots\\ A(n,1) & A(n,1) & \dots & A(n,m)\end{bmatrix}\begin{bmatrix}J(1)\\ J(2)\\ \dots\\ J(m)\end{bmatrix} \tag{7}$$

here n is the number of measurement ($n=201$), and m is the number of line current ($m=99$). The matrix A can be designed for each element, and $A(i,j)=\frac{x(i,j)\cdot\Delta l}{x^2(i,j)+h^2(i,j)}$ is calculated on the basis of the locations of the observation point and the line current. In Equation 7, $\Delta Bz(i)$ at each measurement point can be obtained from the smoothed average CHAMP magnetic field observations, as presented in section 3. Since the matrix A and the observation vector ΔBz are known in Equation 7, we can invert the expression for deriving the sheet current density, $J(j)$, of each jth line current.

Figure 5 shows example plots of average current density profiles within ±45° QDlat at 05 MLT from 2001–2005 and 2005–2009. We can see from Figure 5a that the sheet current density at the magnetic equator, 0° QDlat, during 2001–2005 is about −4.0 mA/m, where the negative sign indicates a westward current direction. Beyond −11° and 17° QDlat the direction of the current switches to eastward. The intensity increases toward higher latitudes reaching about 7.4 (5.6) mA/m in southern (northern) hemisphere. During 2005–2009, the variation characteristics of the current density (see Figure 5b) are similar to that shown in Figure 5a but having different amplitudes. The mean westward current density at 0° QDlat amounts to about −4.0 mA/m, which is comparable to that of 2001–2005, while the eastward current density at −45° (45°) QDlat is 3.3 (1.7) mA/m, is clearly smaller than that of 2001–2005. This indicates that the solar

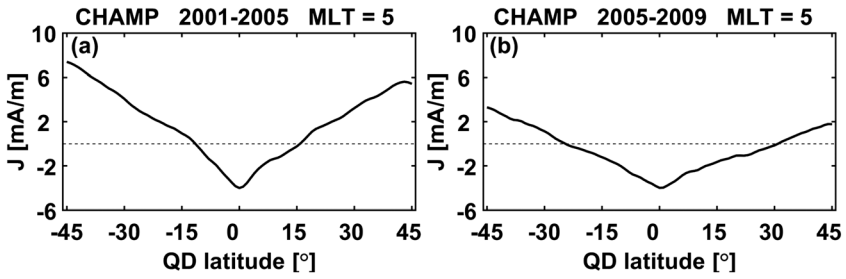

Figure 5. Average latitudinal sheet current density profiles for 05 MLT from (a) 2001–2005 and (b) 2005–2009.

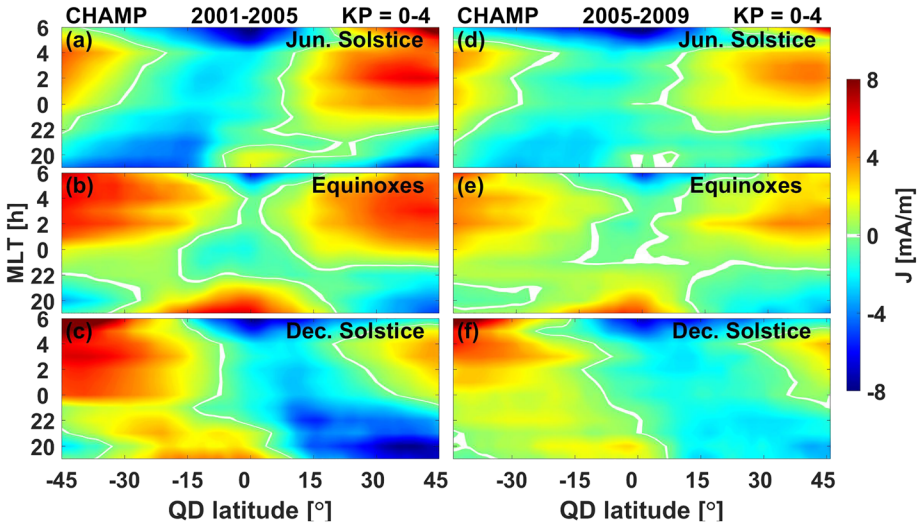

Figure 6. Mean height-integrated zonal current density distribution in latitude versus local time frames, separately for the three seasons from the years 2001–2005 (left) and 2005–2009 (right). Warm colors (yellow, red) represent eastward currents.

activity level has a more significant influence at middle latitudes on the nighttime eastward current in this time sector.

For the verification of our current estimation technique we made some model experiments. As outlined in the supporting information, the magnetic field distribution caused by a rather realistic zonal F-region current sheet, distributed over the height range 185–425 km, was calculated. Samples of the vertical field component were taken along latitudinal profiles at two altitudes, 350 and 400 km, typical for CHAMP. These readings were employed in our inversion (Equation 7). From both profiles we obtained sheet current densities, which are practically identical with the modeled current configuration. This experiment confirms well the used approach.

4.2. Seasonal Dependence of Current Distribution

For investigating the seasonal dependence of the nighttime ionospheric F-region currents, we estimated the current density at middle and low latitudes separately for the three different Lloyd seasons, in which the months May–August represent the June solstice, November–February stand for the December solstice, and the remaining 4 months represent the combined equinoxes. Figure 6 shows the MLT versus QDlat distribution of the nighttime current density during different seasons. The left panel reflects results from the more active years 2001–2005 and the right from the solar minimum years 2005–2009. As in section 3.3, we concentrate on the quiet and moderately activity periods (Kp = 0–4) for studying the seasonal dependence of the ionospheric currents. For the June (December) solstice season, the 131 days centered on 1 July (1 January) are taken into account. For the equinox seasons we combined the two 65-day periods centered on 1 April and 1 October.

From Figure 6 we see that the average height-integrated current density at nighttime is limited to several mA/m during all seasons, with a maximum amplitude of about 8 mA/m. Here warm (yellow, red) colors represent eastward currents and cold (bluish) westward directions. Around June solstice there appears a weak eastward current of about 1 mA/m near the magnetic equator at 19 MLT (see Figure 6a). The latitudinal center of the eastward current shift with progressing nighttime hours toward higher northern latitudes into the summer hemisphere. Similarly, the southern hemisphere midlatitude westward current in the evening shifts toward lower latitudes and reaches the magnetic equator at 06 MLT. During the months around December solstice (see Figure 6c) a mirror image of the June distribution appears. Here the equatorial eastward and midlatitude westward currents shift southward toward later hours. For equinox conditions (see Figure 6b) we obtain a rather symmetric distribution with eastward currents near the equator in the evening and eastward currents at midlatitudes during postmidnight to morning hours. At equinoxes the eastward

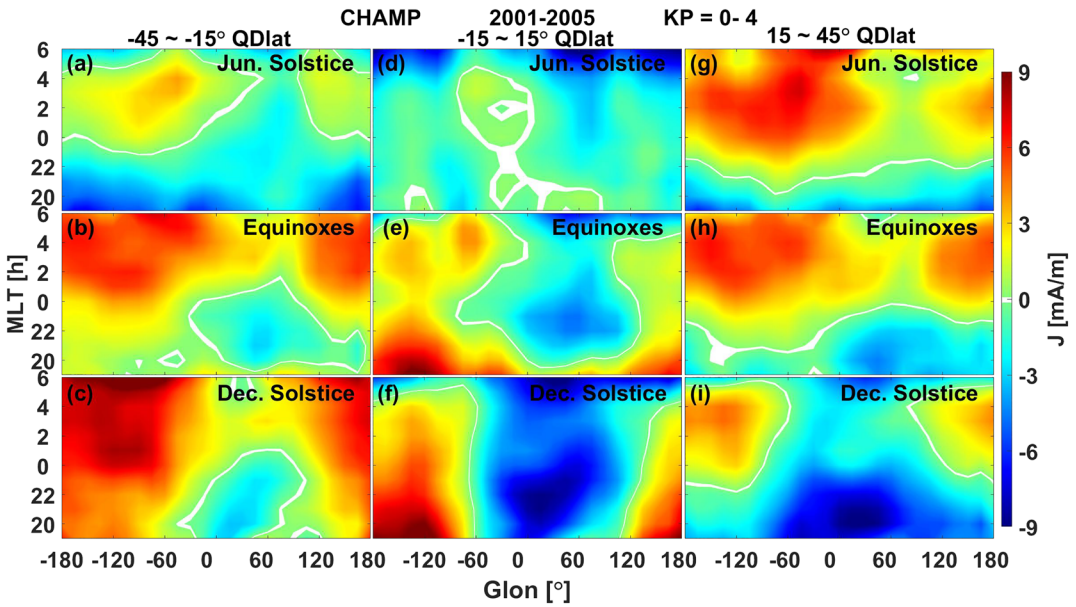

Figure 7. Mean nighttime current density distribution in latitude versus local time frames during the three seasons, separately for (left) southern middle latitude, (middle) low latitude, and (right) northern middle latitude from the years 2001–2005. Warm colors (yellow, red) represent eastward currents.

nighttime currents clearly dominate in the F-region. Weakest current densities are observed during all seasons shortly before midnight (22–24 MLT).

The right column of Figure 6 shows in the same format the average MLT versus QDlat distribution of the current density during 2005–2009. In general, all the prominent features reappear but with a weaker current density. As mentioned in section 3, the average solar radio flux index F10.7 was 76.9 sfu for 2005–2009, compared to the mean F10.7 = 137.4 sfu during 2001–2005. When the current density distributions of both periods are scrutinized, it can be found that the decrease of the current density during 2005–2009 is stronger before midnight. After midnight, it seems that the weakening degree of the current density is not so prominent, especially for the westward current. For example, the low latitude westward current density during early morning hours is almost at the same level in both periods.

4.3. Longitudinal Variation of Current Density

The large number of CHAMP orbits allows for a more detailed investigation of the nighttime current distribution. Figure 6 shows the latitude distribution of the currents averaged over all longitudes, but as a next step we may also look into the longitudinal variations. For that purpose, we have plotted in Figure 7 the longitude versus MLT distribution for three latitude ranges, the southern midlatitudes (left column), low latitudes (middle), and northern midlatitudes (right column) separately for the three seasons. For each latitude range and each season, the measurements are sorted into bins with an interval of 1 hr in MLT and 15° in longitude. In all panels clear longitudinal patterns appear. In the western hemisphere eastward currents dominate. Starting from the Greenwich meridian at evening hours, there is a longitude sector of more westward currents that shifts to more eastern longitudes toward later hours. This westward current component is strongest around December solstice and becomes progressively weaker toward June solstice. In spite of clear differences between the seasons and latitude ranges, there exists a general longitudinal pattern, which may be related to the effect of nonmigrating atmospheric tides.

For performing the tidal analysis, we have averaged the longitudinal variations of all seasons and latitude ranges shown in Figure 7. The result of that exercise is presented in Figure 8a. In a next step longitudinal averages of each MLT hour are subtracted from the bin values. In Figure 8b, the mean-free distribution, a tidal structure emerges already clearly. Since our nighttime data set does only comprise 12 MLT hours, we cannot apply a complete and self-consistent tidal analysis. We have no information about daytime features. Our procedure for estimating the tidal composition is to fit a set of prescribed components to the data. Most

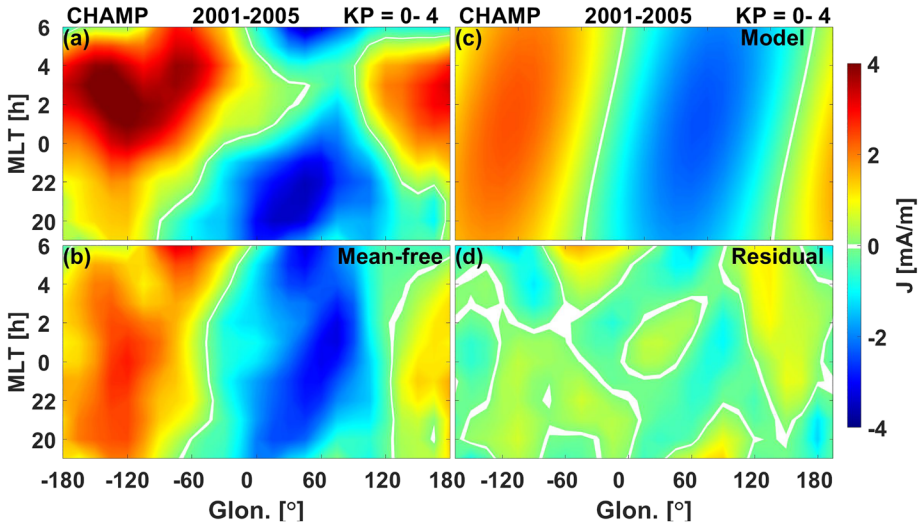

Figure 8. (a) Mean nighttime current density distribution in longitude versus local time frames averaged over all latitudes and seasons; (b) the mean-free distribution is achieved by subtracting the longitudinal means; (c) diurnal tidal model fitting the mean-free observations; (d) remaining residuals. For more details see the text.

promising components are the stationary planetary wave, SPW1, and the symmetric diurnal tide, D0. The modulation of the current, J_{tide} by these tidal components can be expressed as

$$J_{tide} = A_{SPW1}\cos(\lambda - \phi_{SPW1}) + A_{D0}\cos\left[\frac{\pi}{12}\cdot(MLT - \phi_{D0}) - \lambda\right] \quad (8)$$

where A_{SPW1} and A_{D0} are the tidal amplitudes, Φ_{SPW1} and Φ_{D0} are the respective phases, and λ is the longitude. By fitting this function to the data, amplitudes and phases can be estimated. The residuals, data minus tidal model, can be checked for remaining systematic patterns. This tidal analysis is the same as applied in previous publications (e.g., Zhou et al., 2016; Zhou, Lühr, & Alken, 2018; Zhou, Lühr, Xu, et al., 2018).

The best fitting synthetic tidal signal is shown in Figure 8c, and the remaining random residuals in Figure 8d. Our analysis reveals for SPW1 an amplitude (phase) of 1.7 mA/m (234°) and for D0 0.7 mA/m (9.6 hr), respectively. This means, the crest of SWP1 (peak of eastward current) appears at 126°W Glon, and the wave trough (peak of westward current) at 54°E. For D0 we obtain that the wave trough passes the Greenwich longitude at 21.6 MLT. Our analysis implies that the combination of these two wave components can explain the major longitudinal pattern of the nighttime F-region currents at middle and low latitudes and at all seasons. There appear just somewhat different tidal amplitudes at different seasons and latitudes. Without the modulation by the tidal effects the frames in Figure 6 would be sufficient to describe the current distribution.

5. The Nighttime Equatorial Electrojet

A distinct bump appears on the ΔB curves for 05 MLT in Figures 1 and 2 at equatorial latitudes. This can be regarded as the signature of a westward equatorial electrojet in the E-region. So far, there has been no systematic study on the properties of the nighttime EEJ. The technique employed here for determining the EEJ current distribution is based on inverting the scalar magnetic field recordings along the orbit in terms of a series of line currents at E region altitude as described by Alken et al. (2015) and Alken (2020). In this study we follow the same approach as outlined in Zhou, Lühr, Xu, et al. (2018). First the core, crustal, and magnetospheric field contributions are removed from the original field readings. For these purposes we make use of the CHAOS-6 (Finlay et al., 2016), MF7 (Maus et al., 2008), and POMME-6 (Lühr & Maus, 2010) models for subtracting the respective field parts. The contribution of midlatitude Sq currents and unmodeled external fields are filtered out on a track-by-track basis using the procedure detailed in Alken

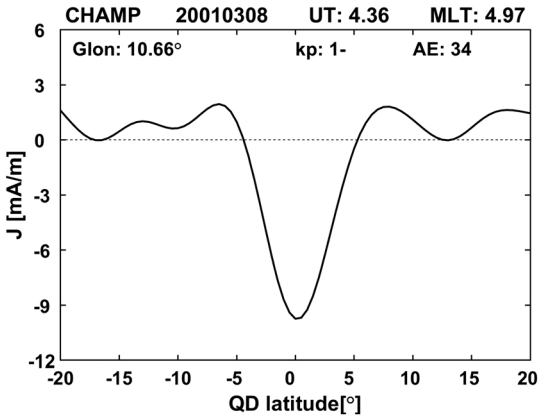

Figure 9. Example of an estimated EEJ height-integrated current density profile. Information about time, location, and activity level are given in the frame.

et al. (2015). The residual magnetic field variations are assumed to represent the clean EEJ signal in the ionospheric E-region. These residuals are the basis for the field inversion to derive latitude profiles of the height-integrated sheet current density profiles about the equator. One example of an EEJ current density profile is shown in Figure 9. Over the magnetic equator such a narrow EEJ profile is typically found during daytime hours. The undulations outside ±10° QDlat are remanences of the background removal procedure. We find a current in westward direction, typical for early morning (05 MLT), and the amplitude of −9.7 mA/m is relatively large for this early morning hour but fits the prevailing solar maximum conditions.

A more significant result can be achieved when current profiles averaged over several years are considered. For the averaging procedure we wanted to make sure that only those profiles are considered that contain EEJ information. According to the characteristics of the EEJ, determined by the distribution of the Cowling conductivity (e.g., Lühr et al., 2004), we identified EEJ events that satisfy three conditions: (1) the peak current densities appear within ±1° about the magnetic equator, (2) the value of the peak amplitude should exceed ±3 mA/m, and (3) the half-maximum width should not exceed ±5° in latitude. Figure 10 presents the mean EEJ profiles of the hour around 05 MLT over the years 2001–2005 and 2005–2009. Here we obtain again the typical narrow EEJ signatures. The difference in mean amplitude we attribute again to the effect of the declining solar cycle. The peak amplitude of −6.9 mA/m from the first period relates to a mean F10.7 = 137 sfu and the −5.3 mA/m from the second to F10.7 = 77 sfu. Graphs shown here can be compared with related magnetic field profiles in Figures 5 and 1 (bottom).

Due to low E-region conductivity the EEJ ceases around 19 MLT, and it cannot form during the night. However, at early morning hours first indications of a westward electrojet are observed. For obtaining a significant picture of the EEJ local time variation, averages of the current density profiles are derived separately for each local time hour. Here the same selection criteria were applied, as described above. These criteria discarded the current density profiles for most of the nighttime hours. From 03 MLT onward we obtain a representative number of valid EEJ profiles. Figure 11 shows hourly averaged current density profiles for the hours 03, 04, 05, and 06 MLT. All the years had to be considered, in order to get enough valid profiles for those hours. The continuous strengthening of a westward EEJ toward later hours is obvious. Derived mean peak amplitudes for the hours 03, 04, 05, and 06 MLT are −3.4, −5.1, −6.2, and −8.6 mA/m, respectively. This represents an almost linear current density increase with local time. It has to be noted here that around 06 MLT already first eastward EEJ events appear. Therefore, that obtained mean value is somewhat diminished.

5.1. Seasonal/Longitudinal Dependence of Nighttime EEJ

So far, only gross averages of the EEJ have been presented. From earlier studies of the daytime EEJ we know that it exhibits distinct longitudinal patterns, which vary from season to season (e.g., Lühr & Manoj, 2013), and the same is true for the equatorial counter electrojet (e.g., Zhou, Lühr, Xu, et al., 2018). For checking the

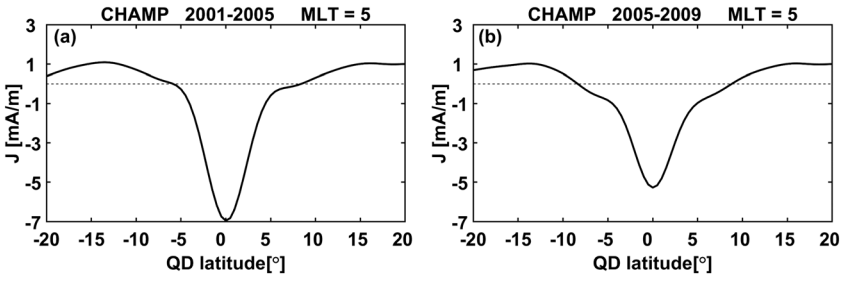

Figure 10. Average latitudinal EEJ height-integrated current density profiles for 05 MLT from (a) 2001–2005 and (b) 2005–2009.

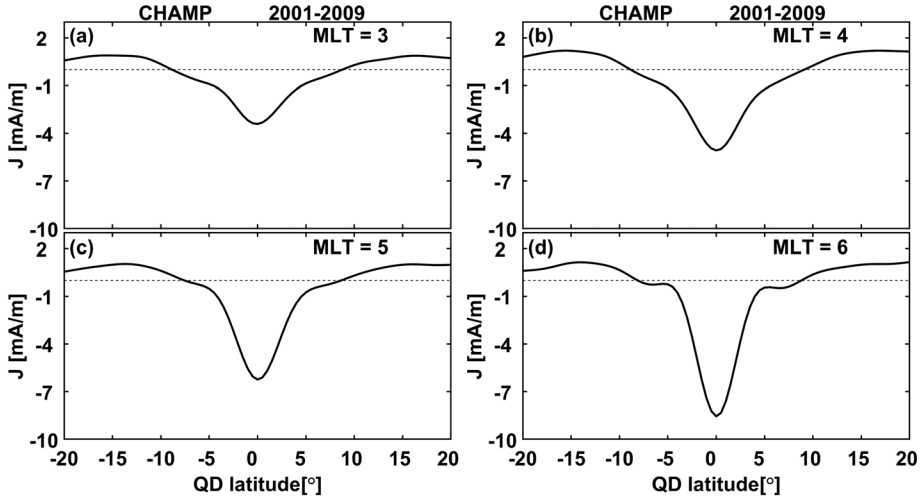

Figure 11. Local time variation of the early morning average EEJ height-integrated current density profiles from 2001–2009.

climatology of the nighttime EEJ we determined the longitudinal variations separately for each month of a year. Figure 12 shows the derived distribution of mean peak current density in a longitude versus Month of Year frame. All the 9 years of CHAMP EEJ estimates were taken into account. We averaged over all the positively selected EEJ profiles from the hours 03, 04, and 05 MLT for calculating the mean peak current densities of each bin. Profiles from 06 MLT have been omitted because they reflect partly already daytime conditions. For reducing the scatter, neighboring bins have been connected by the smoothing function (2), both along the month and the longitude axes.

According to Figure 12 the nighttime EEJs exhibit largest westward current densities around the 0°–60° longitude sector. Conversely, weakest are observed around 120°W Glon. This is in particular true for the June solstice season, when the mean EEJ amplitude almost vanishes in the western sector. Largest westward EEJ amplitudes occur during spring equinox. The longitude distribution found here resemble in many respects that of the nighttime F-region currents shown in Figure 7 and in particular that of the mean-free distribution in Figure 8b. As the cause for those wave-1 longitudinal patterns we identified stationary planetary and diurnal tidal waves. The similar tidal components seem to be responsible for the EEJ amplitude modulations.

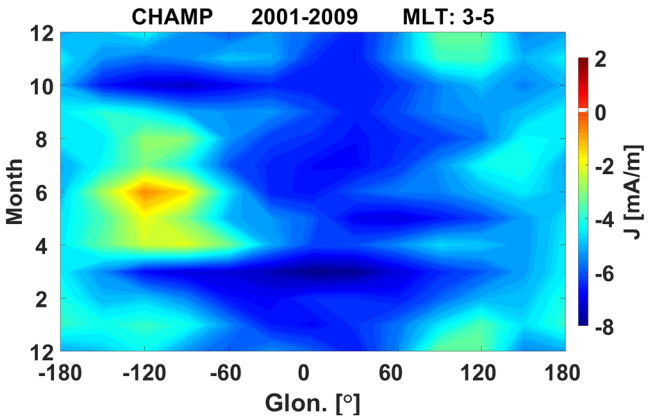

Figure 12. Mean seasonal versus longitudinal distribution of the nighttime EEJ height-integrated current density from the years 2001–2009. Local times considered range from 02:30 to 05:30 MLT.

6. Discussion

In this study we investigated the characteristics of ionospheric currents at nighttime, which are derived by inverting the magnetic signals taken by CHAMP. So far, few studies have focused on them, and none explored them in detail. The precise and high-resolution globally distributed magnetic field data from CHAMP covering a period of 10 years allow the study of various characteristics of these currents. For deriving the ionospheric currents, we first have to remove the main, crustal, and magnetospheric current contributions by means of a comprehensive model like CHAOS-6. These geomagnetic field models are valid for quiet magnetic conditions but show deficiencies during geomagnetic storm-times in representing the magnetospheric fields, as outlined in section 3.2 and shown by Lühr and Zhou (2020). For that reason, this study is limited to quiet and moderately active periods.

Our current estimates are based on a set of east-west oriented line currents. For the F-region currents we chose a separation of 1° in

latitude. From the observed ratio between the ΔBx and ΔBz components we know that CHAMP flew within the F-region current sheet, but the current center was always below the orbit. As a reasonable estimate, we assumed a measurement height of 50 km above the current center. But since we inverted only the ΔBz component in terms of current density distribution, any deviation from the assumed height has little influence on the result, as demonstrated by the validation exercise in the supporting information. Our line current model provides only the zonal component of the F-region current distribution. Therefore, no effort has been made to consider the full current distribution and current continuity.

Things are different for the EEJ estimates. There we know its height in the E-layer and the dominance of the zonal current component. The well-approved inversion procedure applied to the total field readings (Alken, 2020) provides more reliable estimates of that current system. When considering the magnetic contribution of the EEJ to the magnetic field curves (e.g., Figures 1e and 1k) our estimated F-region currents near the magnetic equator during morning hours are somewhat affected by it thus exhibit slightly too negative values at low latitudes (see Figures 5 and 6). In spite of these described limitations the derived currents provide interesting information about the ionospheric dynamics at nighttime.

6.1. Drivers of Nighttime Currents

As mentioned in parts of section 1, the nighttime ionospheric currents are generally composed of contributions from wind-driven currents, pressure gradient currents, gravity-driven currents, and the effect of the polarization electric field that ensures current continuity. At night, after 22 MLT, a large-scale westward electric field is dominating at low latitude (e.g., Fejer, 2011). The gravity-driven currents in the F-region are always directed eastward because of the relative orientation between $\vec{g}$ and $\vec{B}$. They can be expressed as $j_G = n m_i \left(\vec{g} \times \vec{B}\right)/B^2$, here n is the plasma density, m_i is the ion mass, $\vec{g}$ denotes the vector of gravitational acceleration, and $\vec{B}$ is the ambient magnetic field with its magnitude B (e.g., Alken et al., 2017). Due to an angle of 90° between $\vec{g}$ and $\vec{B}$ close to the magnetic equator it is quite limited to low latitudes, hardly extending in latitude beyond the ionization anomaly (EIA). We have removed beforehand the diamagnetic effect from the magnetic field data. Therefore, the pressure gradient currents are largely depressed in our analysis. The zonal wind during nighttime hours is mainly directed eastward, causing upward F-region currents at low latitudes and poleward currents at midlatitudes. Both these current components are not considered here. In addition, we have the meridional winds. These are dominated by the day-to-night atmospheric transport. At midlatitudes these equatorward winds cause eastward F-region currents. Our observations reflect the sum of all those zonal current contributions.

Figure 6 shows the MLT versus QDlat distribution of currents for different seasons. For an interpretation we prefer to start with the distribution during equinoxes. Shortly after sunset eastward currents are observed at low latitudes. These can mainly be attributed to the gravity-driven currents. Already Maus and Lühr (2006) reported an eastward current driven by gravity during 20–22 LT, deduced from the vertical magnetic field component, as observed by CHAMP. In addition, the eastward E-field during the prereversal enhancement (PRE) period can support these currents. Around 22 MLT the low latitude currents fade. At that time the low latitude electric field switches to westward and the EIA density diminishes. Recently Zhong et al. (2019) indicated that the F-region electron density at low latitudes decreases significantly before midnight, especially during equinox seasons. At middle to higher latitudes westward currents are observed during postsunset hours. Such currents have been predicted by Alken et al. (2011), based on TIEGCM electrodynamic modeling, as return currents driven by the polarization electric field.

During postmidnight and early morning hours intense eastward currents appear in both hemispheres at midlatitudes. We attribute these to the effect of meridional winds. The general day-to-night winds are deflected at auroral regions and focused in the postmidnight sector (e.g., Förster et al., 2011, Figure 1). The component perpendicular to the magnetic field of these equatorward winds cause eastward F-region currents, and in addition, the field-aligned wind component can shift plasma along field lines to the topside F-region at middle latitudes. Titheridge (1995) noted the important influence that meridional winds have on the variation of the F region electron density. Both effects support the presence of eastward currents at these times and locations.

During solstice seasons the regions of eastward currents are more shifted to the local summer hemisphere. The region of gravity-driven currents in the evening appears now about 10° in latitude displaced, and the current center shifts toward higher latitudes into the summer hemisphere with increasing night hours. The postsunset return currents are now obviously concentrated in the winter hemisphere. Here westward electric fields leaking out of the subauroral region in the dark hemisphere may support these currents.

Also, the postmidnight eastward currents at midlatitudes flow predominantly in the summer hemisphere. This can well be explained by the higher electron density in that part and the stronger day-to-night wind in the sunlit auroral region (e.g., Lühr et al., 2007). These equatorward winds are turned progressively westward by the Coriolis force when approaching lower latitudes and thus will contribute to the westward large-scale E-field in driving the observed westward low latitude predawn currents.

All the presented arguments for the observed zonal F-region current distribution seem to be valid for both periods of high and low solar activity. The plots in the two columns of Figure 6 agree qualitatively very well with each other, just the current densities are about a factor of 2 smaller during the low activity years 2005–2009.

6.2. Tidal Features of Nighttime Currents

The longitudinal variation of nighttime F-region currents has never been studied before. We could identify a clear pattern as caused by atmospheric tides. Most prominent is the effect of the stationary planetary wave, SPW1, which is centered around 126°W Glon, causing a significant enhancement of eastward currents over most parts of the Pacific Ocean and favoring westward currents over the Eurasian/African sector during all seasons and nighttime hours (see mean-free current distribution in Figure 8b). Currently we have no conclusive explanation of the processes responsible for that stationary planetary wave. We suggest a nonlinear interaction between the migrating diurnal tide, DW1, and the planetary wave, SPW1, that can excite our D0 as secondary product (see, e.g., Hagan & Roble, 2001). The symmetric diurnal tide, D0, represents an enhancement of the westward current (by 0.7 mA/m) around 21:36 UT on global scale and an equivalent global enhancement of eastward current at 09:36 UT. That means, one part of the current modulation, from SPW1, is fixed in longitude and the other, from D0, in UT. The amplitudes of these tides vary with latitude and season, strongest during December months, weakest around June solstice (see Figure 7). But the phase and degree of amplitude modulation stay almost the same during the seasons. From all these observations it may be suggested that the tidal signals are generated by an Earth-fixed driver in the low/middle atmosphere and then propagate upward. The resulting thermospheric winds then modulate the ionospheric currents. Further studies, including numerical modeling, would be helpful for explaining the tidal activity.

6.3. Features of the Nighttime EEJ

Besides the F-region currents we detected also equatorial electrojet currents in the E-region during postmidnight/early morning hours. It is worth noting that in the evening, after 19 MLT, the EEJ ceases and is not detectable by CHAMP through the night. However, at early morning, after 02:30 MLT, first signs of the EEJ can be recognized. Interestingly, already at that time the Cowling channel forms along the equator, which can be concluded from the narrow width of the current band (see Figures 9, 10, and 11). The average latitudinal width at half maximum amounts to about ±3°, comparable to that of the daytime EEJ. This implies a similar E-layer thickness. For the Cowling channel to form the E-layer has to be bounded by poor conductors above and below. The isolator at lower boundary is easy to explain, but what makes the E-layer more conductive, compared to the regions above, at times more than 3 hr before sunrise? What makes these postmidnight hours so special for the built-up of the E-region conductivity compared to the other dark hours before midnight? For answering these questions more studies are needed.

The nighttime EEJ currents flow generally westward. This is consistent with the westward direction of the large-scale electric field during that time of the day (e.g., Fejer, 2011). The continuous growth of EEJ current density toward the morning reflects the increase of E-region conductivity because the background E-field does not change much during those hours. Around 07 MLT the E-field and the EEJ switch from westward to eastward.

By closer inspection of the characteristics we find that the nighttime EEJ shows a pronounced seasonal/longitudinal variation. Quite obvious is the wave-1 longitudinal pattern. Intense westward EEJs

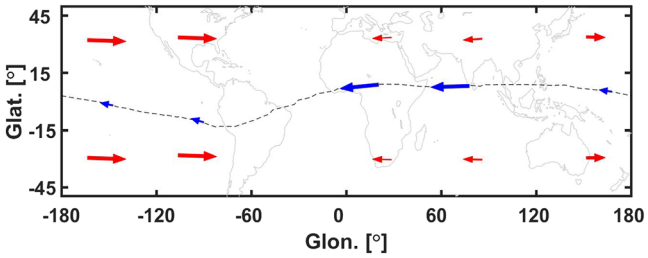

Figure 13. Schematic presentation of the global distribution of the main nighttime currents. Red arrows represent F-region currents and blue the EEJ. Shown is the configuration around 04 MLT for equinox seasons. Quantitative values for the current densities can be derived from Figures 8a and 12 for the F- and E-region, respectively.

are observed during all seasons in a longitude sector centered around 30° Glon (see Figure 12). Weakest nighttime EEJs are found in the sector around −120° Glon and in particular around June solstice months.

The longitudinal variation resembles in some way that of the mean F-region current distribution, as shown in Figure 8. The SPW1 centered at −126° Glon adds in that sector an eastward current component and around 54° Glon a westward current. The tidal winds, assumed to be responsible for the longitudinal F-region current pattern, seem to affect also the EEJ at E-region level. In the African sector they support the westward EEJ, and in the Pacific region they weaken the nighttime EEJ. Interestingly, the wave-1 longitudinal EEJ modulation is most pronounced around June solstice. Already Lühr and Manoj (2013) reported that the eastward daytime electrojet is largely enhanced in the western hemisphere during that season (see their Figure 18). From their tidal analysis (see their Table 5) they revealed that SPW1 is dominating the longitudinal pattern, and it is centered at −122° Glon, which is close to the SPW1 phase of −126° Glon that we derived from F-region current tidal analysis. Around June solstice this planetary wave influences also the EEJ over the whole day, but it is obviously not so effective at E-region altitudes during other seasons away from June, as it is for the F-region nighttime currents.

In general, features of the nighttime EEJ are consistent with its daytime characteristics. Therefore, this part of our study can be regarded as an extension of earlier works on EEJ (e.g., Alken & Maus, 2007; Lühr & Manoj, 2013; Zhou, Lühr, Xu, et al., 2018) toward earlier morning hours.

7. Summary and Conclusions

By interpreting the magnetic field measurements from the CHAMP satellite, the average characteristics of the nighttime ionospheric currents at middle and low latitudes are deduced. On the basis of the vertical magnetic field component variations, the height-integrated sheet current density of the zonal F-region currents has been estimated, by assuming a latitudinal series of line currents. The detailed characteristics of these ionospheric currents throughout the night have been determined, including their spatial, temporal, and seasonal dependences. The main findings of the study can be summarized as follows:

1. Latitudinal profiles of the vertical component and the scalar magnetic field variations, labeled ΔBz and ΔB, indicate that significant nighttime currents are flowing primarily below the CHAMP orbit. From the slope of ΔBz the direction of the zonal F-region currents and their sheet current density can be estimated. Average height-integrated current densities range within ±10 mA/m. The intensity of F-region currents depends on solar activity. Observations suggest a linear variation with the F10.7 flux level. However, the solar activity has no influence on the seasonal, temporal, and spatial patterns of the current distribution. These measurements of magnetic signal provide a first impression of the nighttime current configuration.
2. Shortly after sunset prominent eastward F-region currents are found at low latitudes within ±15° in QDlat. These are believed to be gravity-driven. At middle latitudes westward currents appear. They are clearly enhanced in the winter hemisphere. After 23 MLT the current configuration changes markedly. During the postmidnight hours, we find prominent eastward F-region currents at midlatitudes in both hemispheres. Their intensity is well balanced during equinox seasons but largely enhanced in the summer hemisphere during solstices. We attribute the postmidnight currents to the strong meridional winds in the thermosphere at these local times from the auroral zones to the equator.
3. The F-region currents exhibit a particular longitudinal variation. In the western hemisphere eastward currents are enhanced, and in the eastern part the westward currents. This division can in principle be found at all considered latitudes, local times, and seasons. We attribute this latitudinal pattern to the effect of atmospheric tidal winds. An analysis revealed the stationary planetary wave, SPW1, as the main component modulating the current density. The center of eastward enhancement is located at −126° Glon and that of westward enhancement at 54° Glon. As secondary tide the symmetric diurnal, D0, is

identified. Tidal amplitudes are strongest during December solstice months and weakest around June solstice.

4. During early-morning hours, after 02:30 MLT, first signs of the equatorial electrojet formation appear. The intensity of the westward EEJ current increases toward sunrise hours, where it reaches a typical amplitude of about 10 mA/m. We cannot offer an explanation for the process that enhances selectively the E-region conductivity to significantly higher values than those of adjacent ionospheric layers above and below during the dark hours. Such a configuration is necessary for the Cowling conductivity channel to form near the magnetic equator. The EEJ exhibits a distinct seasonal/longitudinal variation. Similar to the nighttime F-region currents, the westward EEJ is enhanced over Africa and India. Conversely, it is diminished over the Pacific region. This longitudinal modulation is strongest around June solstice. During those months the nighttime EEJ is largely suppressed in the western hemisphere. We suggest that the EEJ longitudinal patterns are caused by the same tidal components as those identified for the F-region currents.

For providing a global overview of the various nighttime ionospheric currents Figure 13 shows schematically the distribution on a map. Illustrated is the situation around 04 MLT for equinox conditions. Red arrows represent midlatitude F-region currents and blue the E-region EEJ. Induced by the tidal influence, intense eastward F-region currents are concentrated above the Pacific Ocean, while amplified westward currents (mainly EEJ) are found over Africa and India. This may indicate that the ocean/continent contrast is supporting the wave-1 tidal structure. More investigations are needed for clarifying that.

Data Availability Statement

The CHAMP magnetic field data (product identifier: CH-ME-3-MAG) are available through Zhou, Lühr, and Alken (2018). Coefficients and software for running the CHAOS-6 model can be downloaded online (http://www.spacecenter.dk/files/magnetic-models/CHAOS-6/), and geomagnetic activity data can be found online (http://omniweb.gsfc.nasa.gov/form/dx1.html).

Acknowledgments

The authors like to thank Robert Pfaff for initiating the discussion about nighttime currents. The CHAMP mission was sponsored by the Space Agency of the German Aerospace Center (DLR) through funds of the Federal Ministry of Economics and Technology. The work of Yun-Liang Zhou is supported by the National Key R&D Program of China (No. 2018YFC1407303) and the National Nature Science Foundation of China (No. 41431073).

References

Alken, P. (2020). Estimating currents and electric fields at low latitudes from satellite magnetic measurements. In M. W. Dunlop, & H. Lühr (Eds.), *Ionospheric multi-spacecraft analysis tools*, *ISSI Scientific Report Series* (Vol. 17, pp. 117–140). Switzerland: Springer Nature.

Alken, P., & Maus, S. (2007). Spatio-temporal characterization of the equatorial electrojet from CHAMP, Ørsted, and SAC-C satellite magnetic measurements. *Journal of Geophysical Research*, *112*, A09305. https://doi.org/10.1029/2007JA012524

Alken, P., Maus, S., Chulliat, A., Vigneron, P., Sirol, O., & Hulot, G. (2015). Swarm equatorial electric field chain: First results. *Geophysical Research Letters*, *42*, 673–680. https://doi.org/10.1002/2014GL062658

Alken, P., Maus, S., Richmond, A. D., & Maute, A. (2011). The ionospheric gravity and diamagnetic current systems. *Journal of Geophysical Research*, *116*, A12316. https://doi.org/10.1029/2011JA017126

Alken, P., Richmond, A. D., & Maute, A. (2017). Ionospheric gravity and pressure gradient current. *Space Science Reviews*, *206*, 451–469. https://doi.org/10.1007/s11214-016-0266-z

Fejer, B. G. (2011). Low latitude ionospheric electrodynamics. *Space Science Reviews*, *158*, 145–166. https://doi.org/10.1007/s11214-010-9690-7

Finlay, C. C., Olsen, N., Kotsiaros, S., Gillet, N., & Toffner-Clausen, L. (2016). Recent geomagnetic secular variation from Swarm and ground observatories as estimated in the CHAOS-6 geomagnetic field model. *Earth, Planets and Space*, *68*(1), 112. https://doi.org/10.1186/s40623-016-0486-1

Förster, M., Haaland, S. E., & Doornbos, E. (2011). Thermospheric vorticity at high geomagnetic latitudes from CHAMP data and its IMF dependence. *Annales de Geophysique*, *29*(1), 181–186. https://doi.org/10.5194/angeo-29-181-2011

Hagan, M. E., & Roble, R. G. (2001). Modeling the diurnal tidal variability with the National Center for Atmospheric Research thermosphere-ionosphere-mesosphere-electrodynamics general circulation model. *Journal of Geophysical Research*, *106*(A11), 24,869–24,882. https://doi.org/10.1029/2001JA000057

Heelis, R. A. (2004). Electrodynamics in the low and middle latitude ionosphere: A tutorial. *Journal of Atmospheric and Solar - Terrestrial Physics*, *66*(10), 825–838. https://doi.org/10.1016/j.jastp.2004.01.034

Kelley, M. (2009). *The Earth's ionosphere: Plasma physics and electrodynamics*, 2nd. Boston: Academic Press (Elsevier).

Le, G., Burke, W. J., Pfaff, R. F., Freudenreich, H., Maus, S., & Lühr, H. (2011). C/NOFS measurements of magnetic perturbations in the low-latitude ionosphere during magnetic storms. *Journal of Geophysical Research*, *116*, A12230. https://doi.org/10.1029/2011JA017026

Lühr, H., Kervalishvili, G., Rauberg, J., & Stolle, C. (2016). Zonal currents in the F region deduced from Swarm constellation measurements. *Journal of Geophysical Research: Space Physics*, *121*, 638–648. https://doi.org/10.1002/2015JA022051

Lühr, H., & Manoj, C. (2013). The complete spectrum of the equatorial electrojet related to solar tides: CHAMP observations. *Annales de Geophysique*, *31*(8), 1315–1331. https://doi.org/10.5194/angeo-31-1315-2013

Lühr, H., & Maus, S. (2010). Solar cycle dependence of quiet-time magnetospheric currents and a model of their near-Earth magnetic fields. *Earth, Planets and Space*, *62*(10), 843–848. https://doi.org/10.5047/eps.2010.07.012

Lühr, H., Maus, S., & Rother, M. (2004). The noon-time equatorial electrojet, its spatial features as determined by the CHAMP satellite. *Journal of Geophysical Research*, *109*, A01306. https://doi.org/10.1029/2002JA009656

Lühr, H., Rentz, S., Ritter, P., Liu, H., & Häusler, K. (2007). Average thermospheric wind patterns over the polar regions, as observed by CHAMP. *Annales de Geophysique*, *25*(5), 1093–1101. www.ann-geophys.net/25/1093/2007/, https://doi.org/10.5194/angeo-25-1093-2007

Lühr, H., Rother, M., Maus, S., Mai, W., & Cooke, D. (2003). The diamagnetic effect of the equatorial Appleton anomaly: Its characteristics and impact on geomagnetic field modelling. *Geophysical Research Letters*, *30*(17), 1906. https://doi.org/10.1029/2003GL017407

Lühr, H., Xiong, C., Olsen, N., & Le, G. (2017). Near-Earth magnetic field effects of large-scale magnetospheric currents. *Space Science Reviews*, *206*(1-4), 521–545. https://doi.org/10.1007/s11214-016-0267-y

Lühr, H., & Zhou, Y.-L. (2020). Residuals to the CHAOS-6 geomagnetic field model caused by magnetospheric currents during enhanced magnetic activity. *Geochemistry, Geophysics, Geosystems*, *21*, e2020GC008976. https://doi.org/10.1029/2020GC008976

Maeda, H., Iyemori, T., Araki, T., & Kamei, T. (1982). New evidence of a meridional current system in the equatorial ionosphere. *Geophysical Research Letters*, *9*(4), 337–340. https://doi.org/10.1029/GL009i004p00337

Maus, S., & Lühr, H. (2006). A gravity-driven electric current in the Earth's ionosphere identified in CHAMP satellite magnetic measurements. *Geophysical Research Letters*, *33*, L02812. https://doi.org/10.1029/2005GL024436

Maus, S., Yin, F., Lühr, H., Manoj, C., Rother, M., Rauberg, J., et al. (2008). Resolution of direction of oceanic magnetic lineations by the sixth-generation lithospheric magnetic field model from CHAMP satellite magnetic measurements. *Geochemistry, Geophysics, Geosystems*, *9*, Q07021. https://doi.org/10.1029/2008GC001949

Maute, A., & Richmond, A. (2017). F-region dynamo simulations at low and mid-latitude. *Space Science Reviews*, *206*, 471–493. https://doi.org/10.1007/s11214-016-0262-3

Reigber, C., Lühr, H., & Schwintzer, P. (2002). CHAMP mission status. *Advances in Space Research*, *30*(2), 129–134. https://doi.org/10.1016/S0273-1177(02)00276-4

Richmond, A. (1979). Ionospheric wind dynamo theory: A review. *Journal of Geomagnetism and Geoelectricity*, *31*(3), 287–310. https://doi.org/10.5636/jgg.31.287

Richmond, A. D. (1995). Ionospheric electrodynamics using magnetic apex coordinates. *Journal of Geomagnetism and Geoelectricity*, *47*(2), 191–212. https://doi.org/10.5636/jgg.47.191

Rishbeth, H. (1971a). The F-layer dynamo. *Planetary and Space Science*, *19*(2), 263–267. https://doi.org/10.1016/0032-0633(71)90205-4

Rishbeth, H. (1971b). Polarization fields produced by winds in the equatorial F-region. *Planetary and Space Science*, *19*(3), 357–369. https://doi.org/10.1016/0032-0633(71)90098-5

Rother, M. & Michaelis, I. (2019): CH-ME-3-MAG — CHAMP 1 Hz combined magnetic field time series (Level 3). GFZ Data Service. https://doi.org/10.5880/GFZ.2.3.2019.004

Shore, R. M., Whaler, K. A., Macmillan, S., Beggan, C., Olsen, N., Spain, T., & Aruliah, A. (2013). Ionospheric midlatitude electric current density inferred from multiple magnetic satellites. *Journal of Geophysical Research: Space Physics*, *118*, 5813–5829. https://doi.org/10.1002/jgra.50491

Titheridge, J. E. (1995). Winds in the ionosphere—A review. *Journal of Atmospheric and Terrestrial Physics*, *57*(14), 1681–1714. https://doi.org/10.1016/0021-9169(95)00091-F

Tozzi, R., Pezzopane, M., DeMichelis, P., & Piersanti, M. (2015). Applying a curl-B technique to Swarm vector data to estimate night-time F-region current densities. *Geophysical Research Letters*, *42*, 6162–6169. https://doi.org/10.1002/2015GL064841

Zhong, J., Lei, J., Yue, X., Luan, X., & Dou, X. (2019). Middle-latitudinal band structure observed in the nighttime ionosphere. *Journal of Geophysical Research: Space Physics*, *124*, 5857–5873. https://doi.org/10.1029/2018JA026059

Zhou, Y.-L., Lühr, H., & Alken, P. (2018). The sidebands of the equatorial electrojet: General characteristic of the westward currents, as deduced from CHAMP. *Journal of Geophysical Research: Space Physics*, *123*, 1457–1476. https://doi.org/10.1002/2017JA024687

Zhou, Y.-L., Lühr, H., Alken, P., & Xiong, C. (2016). New perspectives on equatorial electrojet tidal characteristics derived from the Swarm constellation. *Journal of Geophysical Research: Space Physics*, *121*, 7226–7237. https://doi.org/10.1002/2016JA022713

Zhou, Y.-L., Lühr, H., Xu, H.-W., & Alken, P. (2018). Comprehensive analysis of the counter equatorial electrojet: Average properties as deduced from CHAMP observations. *Journal of Geophysical Research: Space Physics*, *123*, 5159–5181. https://doi.org/10.1029/2018JA025526